nature geoscience

SUPPLEMENTARY INFORMATION

https://doi.org/10.1038/s41561-018-0297-z

In the format provided by the authors and unedited.

Early and persistent supershear rupture of the 2018 magnitude 7.5 Palu earthquake

Han Bao[1], Jean-Paul Ampuero[2,3]*, Lingsen Meng[1], Eric J. Fielding[4], Cunren Liang[3], Christopher W. D. Milliner[4], Tian Feng[1] and Hui Huang[1]

[1]Earth, Planetary and Space Sciences, University of California, Los Angeles, CA, USA. [2]Université Côte d'Azur, IRD, CNRS, Observatoire de la Côte d'Azur, Géoazur, France. [3]California Institute of Technology, Seismological Laboratory, Pasadena, CA, USA. [4]Jet Propulsion Laboratory, California Institute of Technology, Pasadena, CA, USA. *e-mail: ampuero@geoazur.unice.fr

Supplementary material of "Early and persistent supershear rupture of the 2018 magnitude 7.5 Palu earthquake"

Han Bao[1], Jean-Paul Ampuero[2,3], Lingsen Meng[1], Eric J. Fielding[4], Cunren Liang[3], Christopher W. D. Milliner[4], Tian Feng[1], Hui Huang[1]

1. Earth, Planetary and Space Sciences, University of California, Los Angeles, California. USA

2. Université Côte d'Azur, IRD, CNRS, Observatoire de la Côte d'Azur, Géoazur, France

3. California Institute of Technology, Seismological Laboratory, Pasadena, California, USA

4. Jet Propulsion Laboratory, California Institute of Technology, Pasadena, California, USA

Corresponding author

J. P. Ampuero, ampuero@geoazur.unice.fr

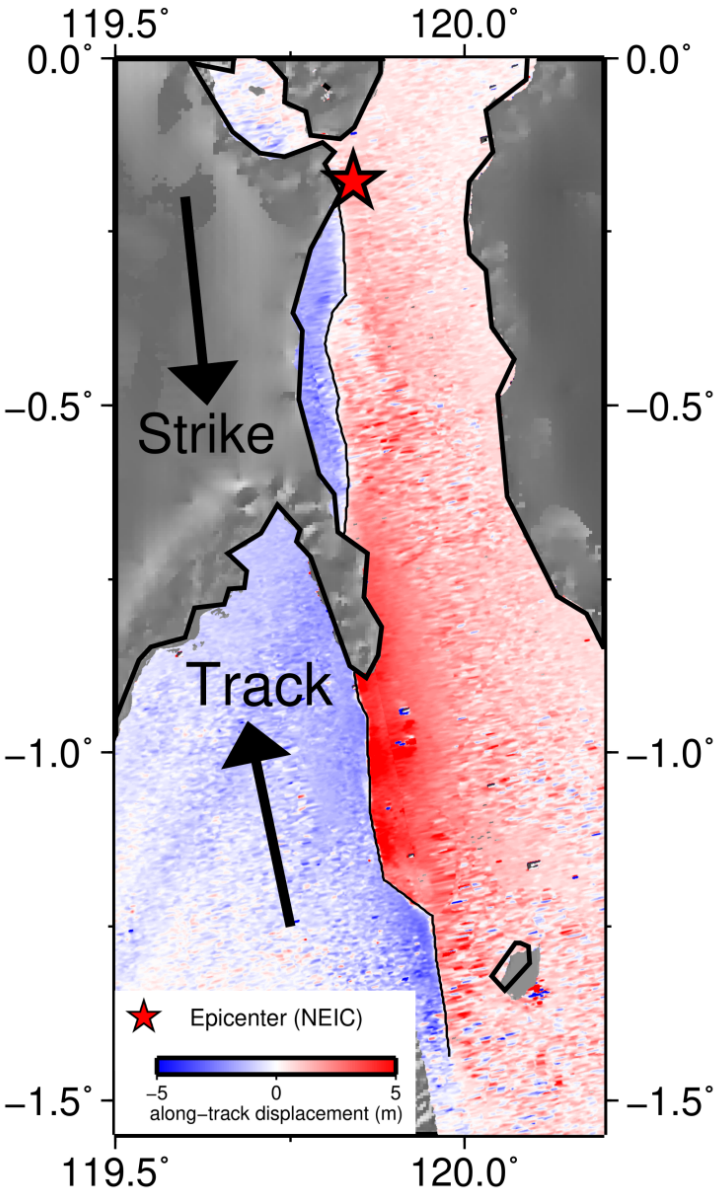

Figure S1. High-resolution along-track displacements from ALOS-2 SAR offsets (colored image on land) and bathymetry (gray background offshore). The arrow labeled as “track” indicates the direction of the measurement, -11.7°. The red star denotes the NEIC epicenter of the Palu earthquake. This is the same as Figure 1a but plotted without the back-projection results, to show without obstruction the interpretation of the surface rupture trace from the SAR results.

Sensor	Sensor type	date1	date2	frames	beam
ALOS-2 path 127	SAR	2018/08/08	2018/10/03	7160–7170	SM3 F2-7
ALOS-2 path 126	SAR	2018/08/17	2018/10/12	7150–7190	SM3 F2-5
Sentinel-2	Optical	2018/03/20	2018/10/25	N/A	N/A
Planet labs	Optical	2018/09/27	2018/10/02	N/A	N/A

Table S1. JAXA ALOS-2 PALSAR-2 scenes and optical data used in the pixel offset analysis.

AU array	Magnitude	Relocated locations		NEIC location		GFZ location		BP location		BP location with Calibration	
		lat	lon	lat	lon	lat	lon	lat	lon	lat	lon
2018-09-28 08:24:58	5.0	-0.363	119.785	-0.342	119.871	-0.330	119.91	-0.107	119.825	-0.309	119.795
2018-09-28 07:00:01	6.1	-0.423	119.750	-0.398	119.76	-0.450	119.78	-0.147	119.825	-0.359	119.764
2018-09-28 12:27:33	5.1	-0.323	119.925	-0.464	119.915	-0.440	119.89	-0.188	119.901	-0.381	119.946
2018-10-01 23:46:39	5.2	-0.623	119.875	-0.675	119.877	-0.650	119.92	-0.390	119.825	-0.557	119.885
2018-09-28 10:50:25	5.7	-0.768	119.965	-0.754	119.947	-0.700	120.05	-0.471	119.916	-0.673	119.976
2018-09-28 10:16:49	5.7	-0.783	120.005	-0.887	120.027	-0.850	120.04	-0.511	119.976	-0.713	120.007
2018-09-28 10:25:04	5.8	-1.0681	119.980	-1.062	119.96	-0.930	120.02	-0.936	119.825	-0.996	119.916
2018-09-28 13:39:44	5.2	-1.328	119.945	-1.414	119.965	NaN	NaN	-1.238	119.825	-1.358	119.976
2018-09-28 11:06:51	5.2	-1.518	120.075	-1.493	120.025	-1.480	120.06	-1.425	119.976	-1.501	120.037
2018-09-28 10:47:44	5.1	Low signal coherence									
2018-09-28 10:39:03	5.4	Relocation error too large (>20km)									

Table S2. Locations of two foreshocks and all (M>5.0) aftershocks in the vicinity of the mainshock rupture region (by Oct 08, 2018). The first 9 events are used in the slowness calibration of the back-projection (AU array). The root-mean-square (RMS) error between the BP locations and the relocated aftershock locations is reduced from 25.5 km to 7.6 km by the slowness calibration.

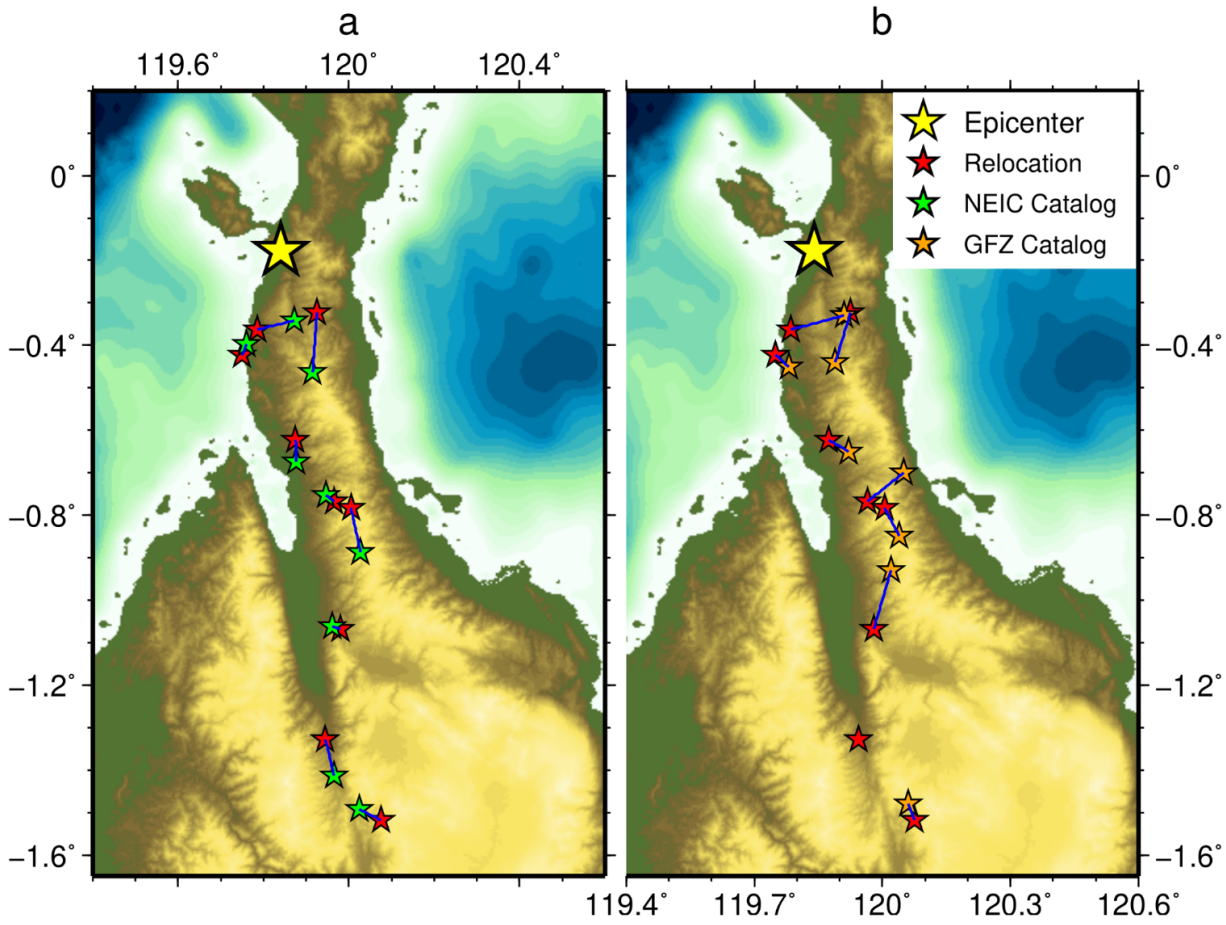

Figure S2. Comparison of aftershocks' relocations and catalog locations. Yellow star is the epicenter location. Red stars are relocated locations. Green stars are NEIC catalog locations. Orange stars are GFZ locations. These locations can be inferred in Table S2.

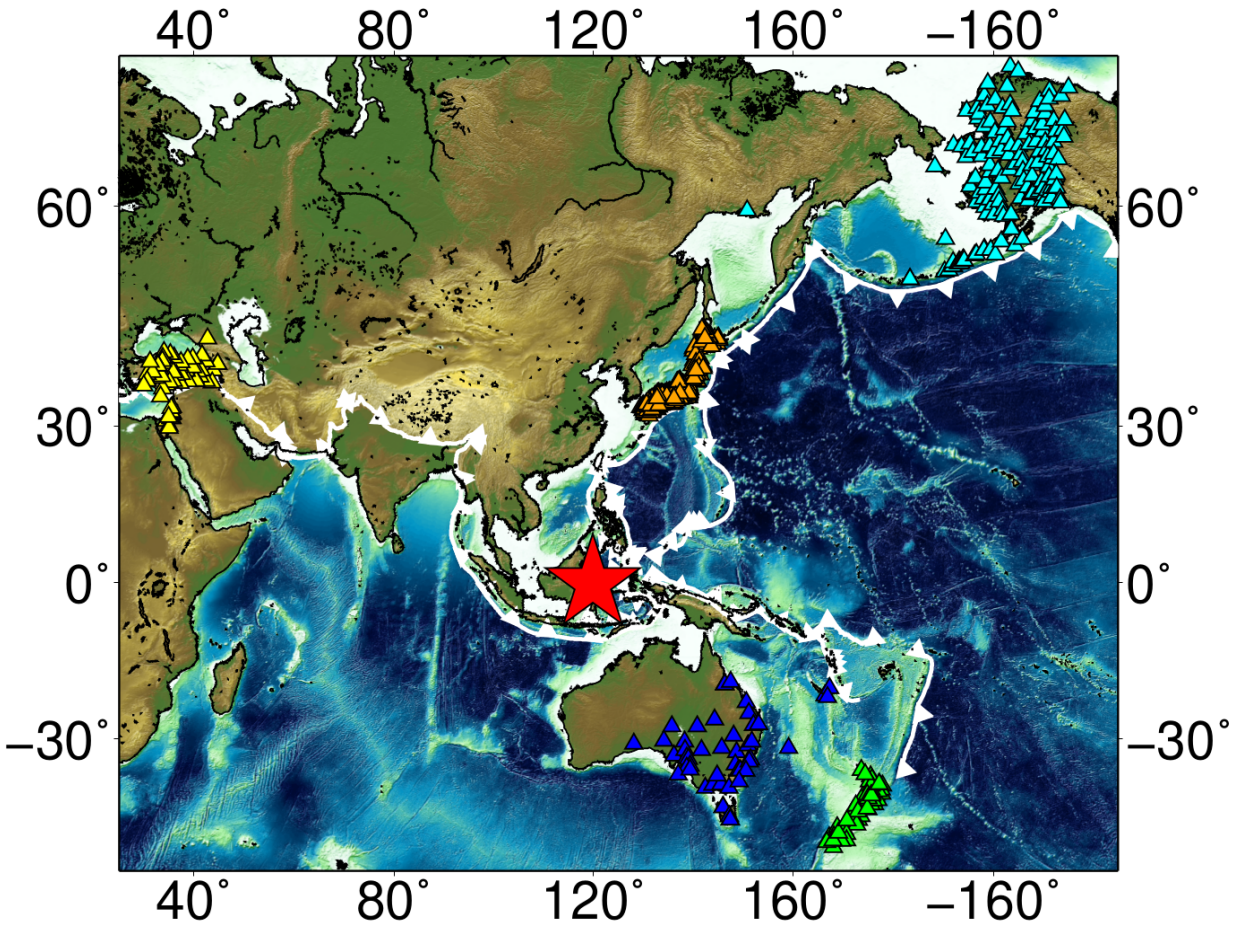

Figure S3. Teleseismic arrays considered for the back-projection analysis. The colored triangles represent the seismic stations from arrays in Turkey (yellow), Australia (blue), New Zealand (green), Japan (orange), and Alaska (cyan). The red star denotes the location of the Mw7.5 Palu earthquake.

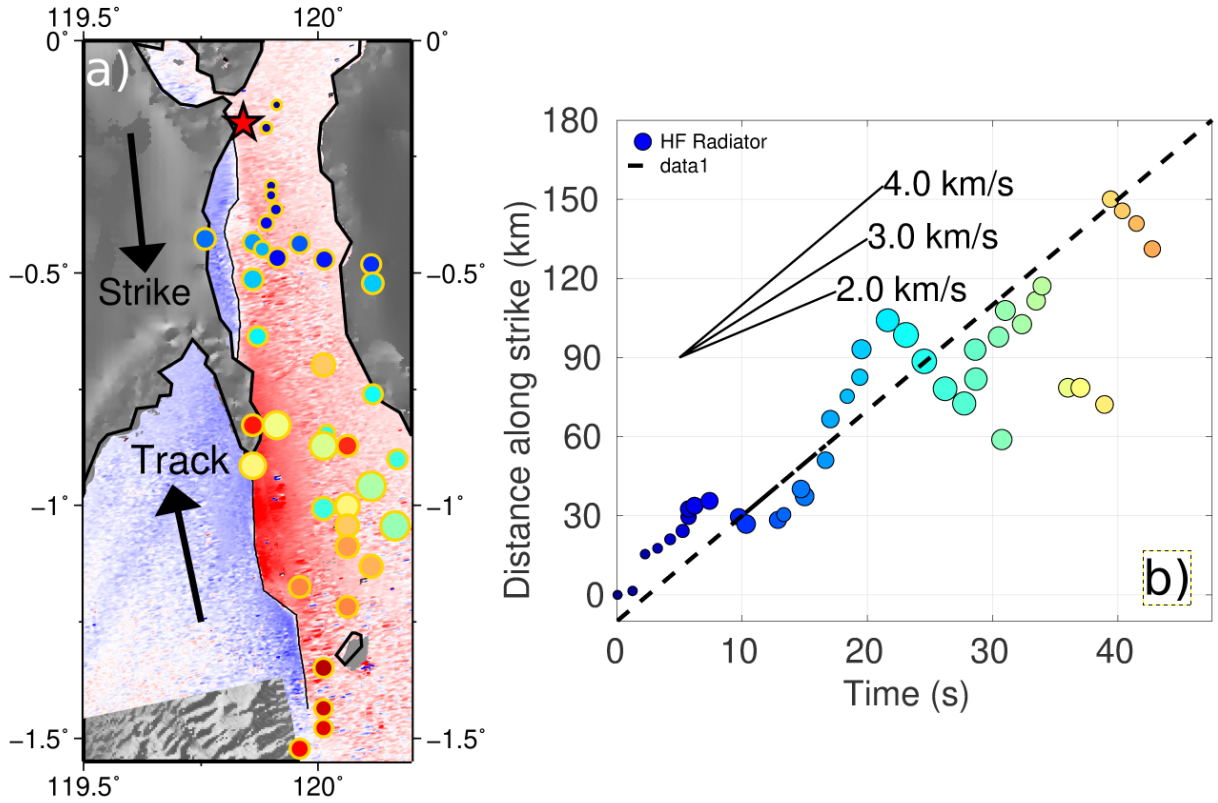

Figure S4. Rupture imaging by Slowness-Enhanced Back-Projection (SEBP) of data recorded by the Turkish array. **a)** Circles denote the high-frequency (0.5~2 Hz) radiators, with size proportional to relative energy (beamforming power) and color representing rupture time with respect to the mainshock origin time. Note that the spatial bias along the west-east direction on the southern part of the rupture is not perfectly corrected by our aftershock calibration (see Figure S5). **b)** Along-strike location and timing of radiators. Time is relative to rupture origin time. Location is the horizontal position relative to the hypocenter, projected along the average strike direction (174°). The solid lines indicate reference rupture speeds. The dashed line is a linear regression of the leading front radiators. The average rupture speed estimate and its standard deviation are $4.08 \pm 0.21\ km/s$.

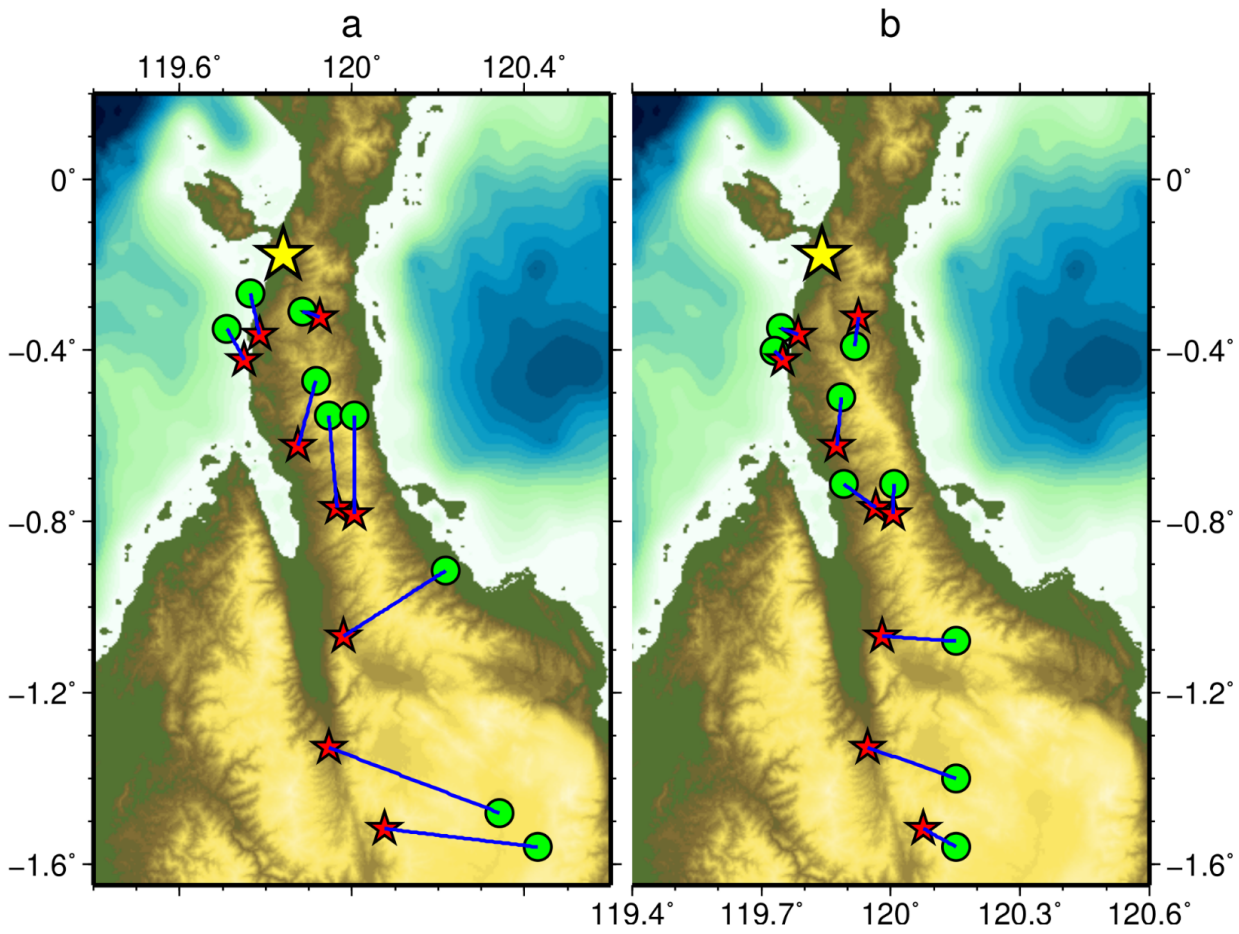

Figure S5. Slowness calibration of back-projection based on aftershock data for the Turkish array. BP-inferred (green circles) and relocated (red stars) locations of 9 M5.1+ aftershocks spanning the rupture region, before (a) and after (b) the slowness calibration. The root-mean-square error (RMSE) is decreased by slowness calibration from 27.1 km to 12.4 km.

EU array	Magnitude	Relocated locations		BP location		BP location with Calibration	
		lat	lon	lat	lon	lat	lon
2018-09-28 08:24:58	5.0	-0.363	119.785	-0.267	119.764	-0.349	119.744
2018-09-28 07:00:01	6.1	-0.423	119.750	-0.350	119.710	-0.401	119.731
2018-09-28 12:27:33	5.1	-0.323	119.925	-0.309	119.885	-0.390	119.916
2018-10-01 23:46:39	5.2	-0.623	119.875	-0.471	119.916	-0.511	119.885
2018-09-28 10:50:25	5.7	-0.768	119.965	-0.553	119.946	-0.713	119.891
2018-09-28 10:16:49	5.7	-0.783	120.005	-0.552	120.006	-0.713	120.007
2018-09-28 10:25:04	5.8	-1.0681	119.980	-0.915	120.218	-1.077	120.152
2018-09-28 13:39:44	5.2	-1.328	119.945	-1.481	120.341	-1.359	120.151
2018-09-28 11:06:51	5.2	-1.518	120.075	-1.561	120.431	-1.560	120.150
2018-09-28 10:47:44	5.1	Low signal coherence					
2018-09-28 10:39:03	5.4	Relocation error too large (>20km)					

Table S3. Locations of two foreshocks and all aftershocks in the vicinity of the mainshock rupture region (by Oct 08, 2018). The first 9 events are used in the slowness calibration of the back-projection (Turkish array). The root-mean-square (RMS) error between the BP locations and the relocated locations is reduced from 27.1 km to 12.4 km.

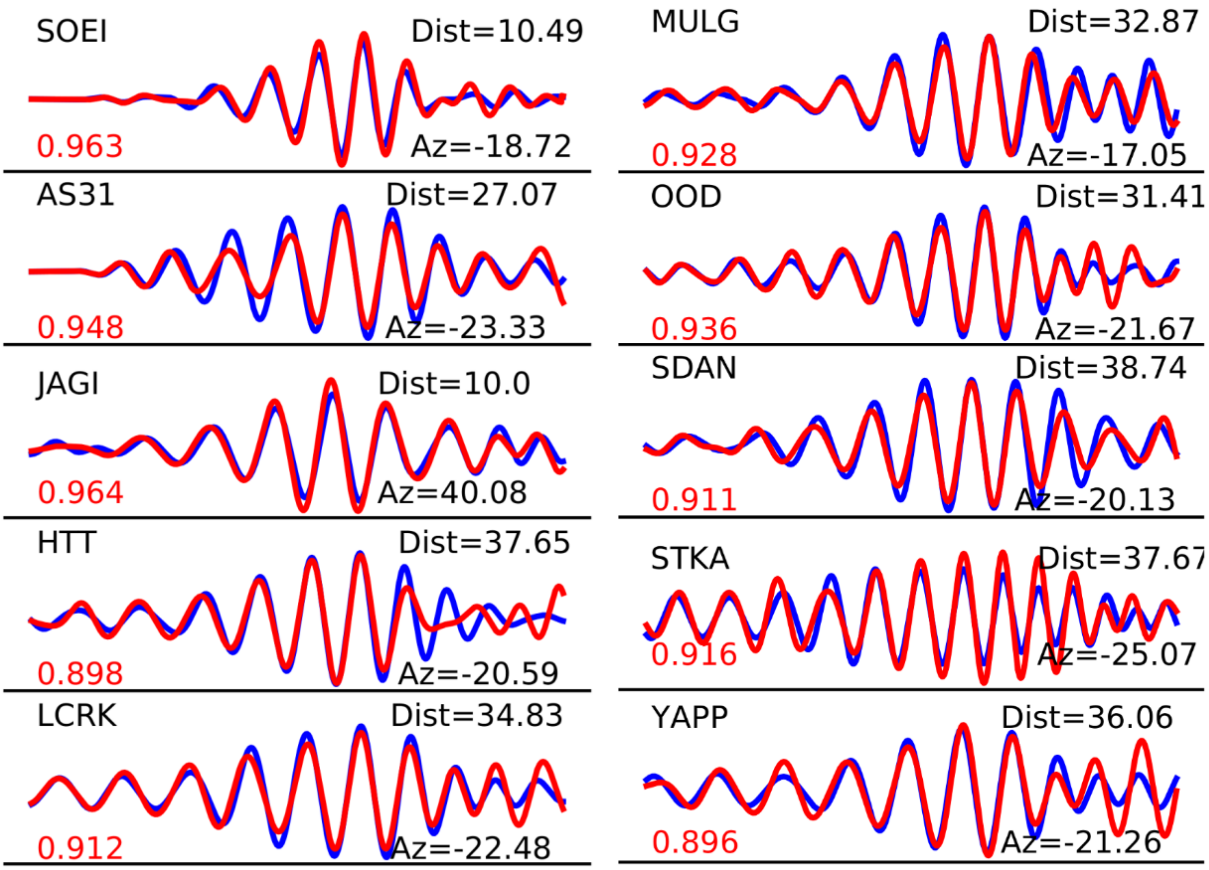

Figure S6. Rayleigh wave vertical displacement seismograms of mainshock (blue) and foreshock (red) in the 15–25 s period range recorded at stations located in Mach cones. Station name, azimuth relative to the rupture direction (Az), hypocentral distance (Dist), and correlation coefficient (red) are shown for each station. Station locations are shown in Fig. S8.

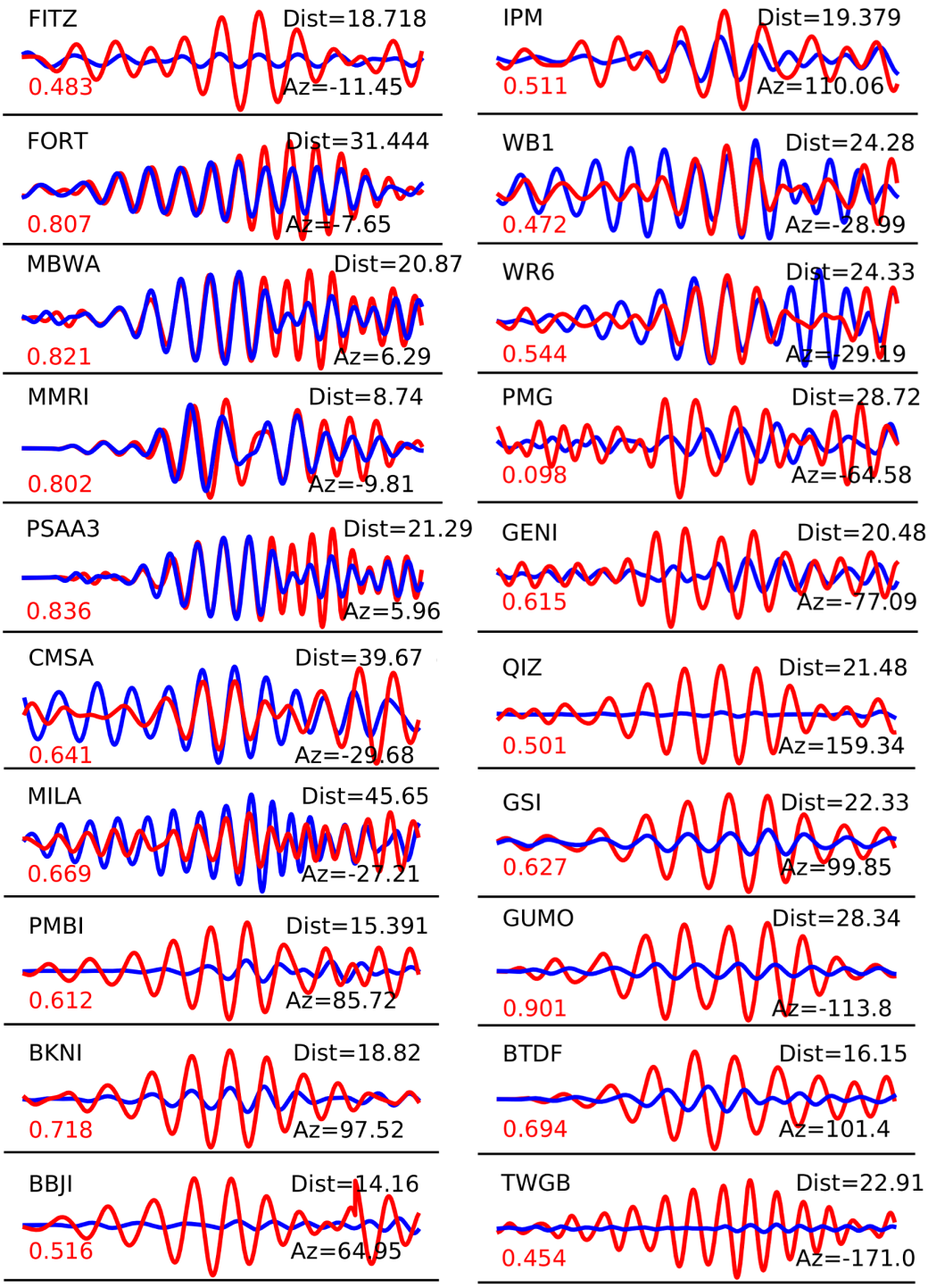

Figure S7. Rayleigh wave displacement seismograms of mainshock (blue) and foreshock (red) in the 15–25 s period range recorded at stations located out of Mach cones. Station name,

azimuth (Az) relative to the rupture direction, hypocentral distance (Dist), and correlation coefficient (red decimal) are shown for each station. Station locations are shown in Fig. S7.

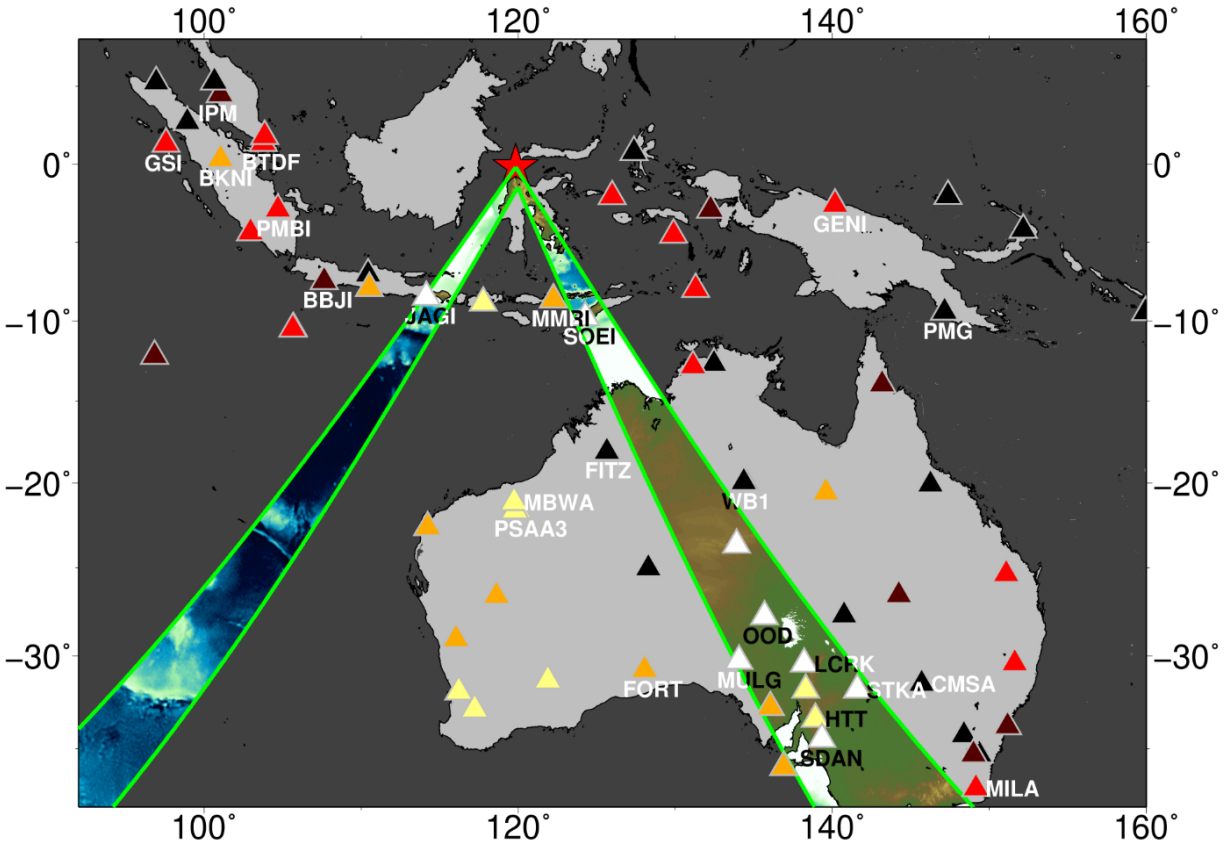

Figure S8. Same as Fig. 3, but showing names of stations whose wave resemblance are shown in Fig. S6 and Fig. S7.

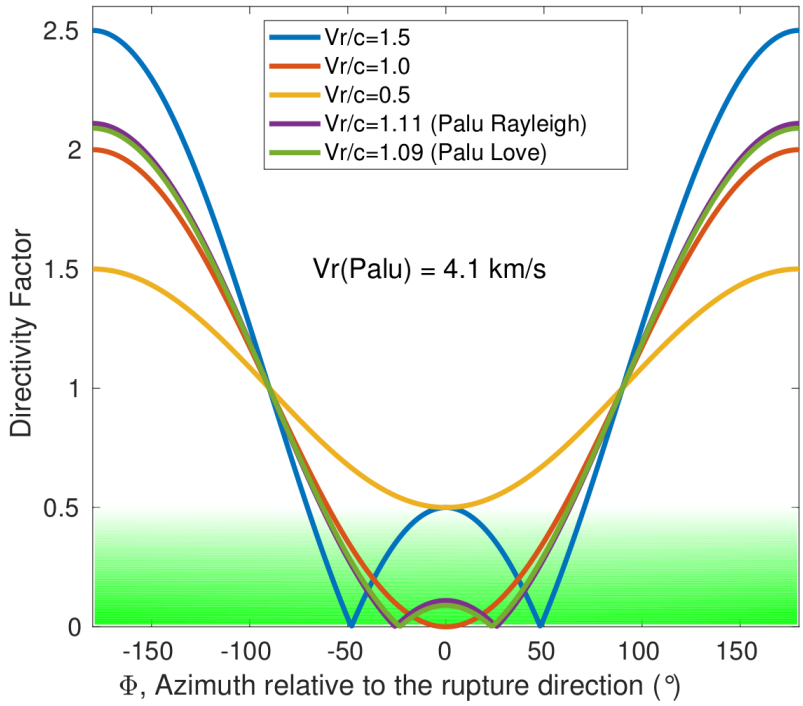

Figure S9. Absolute value of the directivity factor D(Φ)=1-cos(Φ)*Vr/c as a function of azimuth Φ relative to the rupture direction, for different ratios of rupture speed Vr to wave speed c. The bandpass filtered waveforms of a mainshock and a co-located foreshock are similar if the apparent corner frequency of the mainshock, 1/(|D|*T) where T is the rupture duration, is substantially higher than the dominant frequency 1/T0 of the filtered waveforms. In our analysis of the Palu earthquake T~40 s and T0~20 s, thus the condition for similarity is |D(Φ)|<<0.5. This condition is met at azimuths for which the |D(Φ)| curve in this figure falls within the darker green band. For sufficiently fast sub-Rayleigh ruptures (red curve), waveform similarity is expected to be maximal in the direction of rupture. For supershear ruptures (blue, purple and green curves), waveform similarity is maximal on the Mach cones, i.e. at the two azimuths where D(Φ)=0, but it can be high also in between if the rupture speed is not too fast (purple and green curves, corresponding to the Palu earthquake speed compared to Rayleigh and Love waves, respectively).

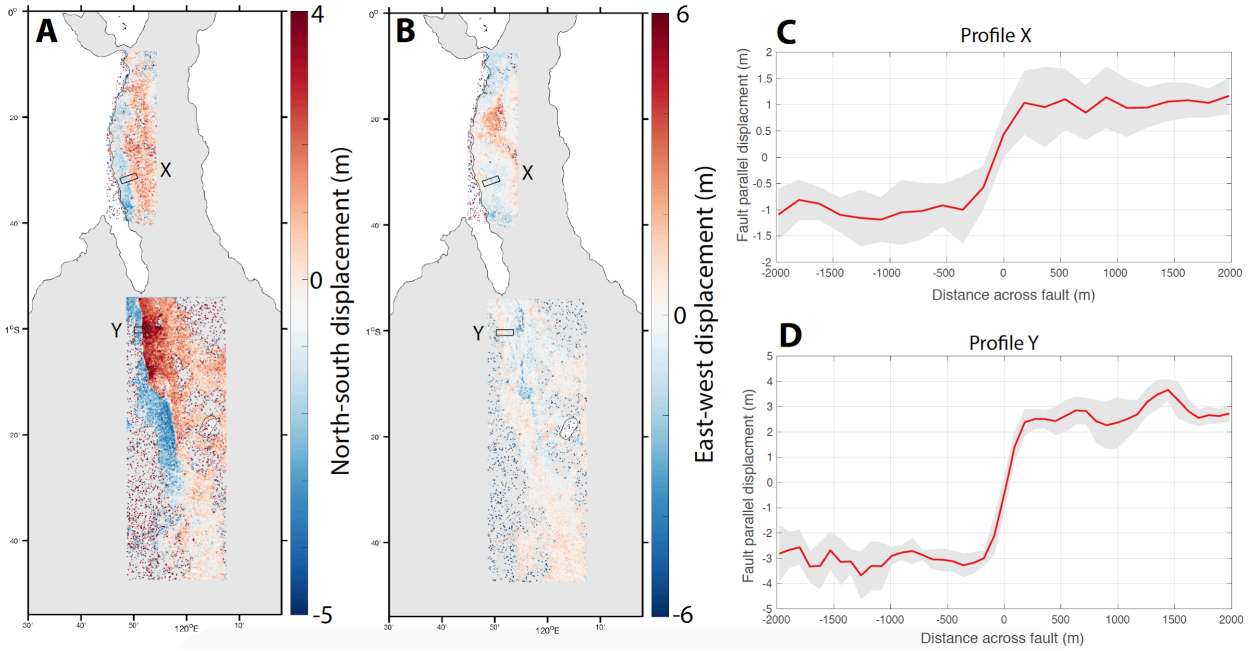

Fig. S10. High-resolution optical pixel tracking results from Sentinel 2 and Planet Labs imagery. A Surface displacement resolved into the north-south direction (a) and east-west direction (b). Decorrelation occurs due to changes in scene that could not be matched between acquisitions, mostly from clouds and regions of water over the Makaasar Strait. c) and d) show fault parallel displacements on across-fault stacked profiles extracted from the correlation maps from the north and south areas, respectively, shown by boxes in a) and b). Fault slip is measured as the total discontinuity of the surface motion across the fault.

Supplementary text. **Spatial uncertainty estimation of the slowness-enhanced back-projection**

This uncertainty estimation follows the posterior model uncertainty estimation based on error propagation theory (Menke, 2012).

1. The calculation of the slowness error (Meng et al. 2016) is basically a least square inversion problem.

$$\Delta \mathrm{T} = \mathrm{G} \cdot dS \qquad \textit{Eq. 1)}$$

where

$$\Delta T = \begin{bmatrix} \Delta \mathrm{t}_{1j} \\ \Delta \mathrm{t}_{2j} \\ \vdots \\ \Delta \mathrm{t}_{ij} \\ \vdots \\ \Delta \mathrm{t}_{mj} \end{bmatrix}, \qquad G = \begin{bmatrix} \Delta \mathrm{X}_1 & \Delta \mathrm{Y}_1 \\ \Delta \mathrm{X}_2 & \Delta \mathrm{Y}_1 \\ \vdots & \vdots \\ \Delta \mathrm{X}_i & \Delta \mathrm{Y}_i \\ \vdots & \vdots \\ \Delta \mathrm{X}_m & \Delta \mathrm{Y}_m \end{bmatrix}, \qquad dS = \begin{bmatrix} dS_{jx} \\ dS_{jy} \end{bmatrix},$$

where $\Delta \mathrm{t}_{ij}$ is the travel time error from aftershock i to station j. It is calculated from its catalog location (red stars) and BP-inferred location (green circles). $\Delta \mathrm{X}_i$ and $\Delta \mathrm{Y}_i$ are the longitude and latitude distance between the catalog location and BP inferred location of aftershock i, and m denotes the number of aftershocks. dS_{1x} and dS_{1y} are the longitudinal and latitudinal slowness errors of station j that need to be solved, which will be adopted throughout the entire rupture region.

2. dS_j can be solved by least square inversion:

$$dS^{est} = G^{-g} \cdot \mathrm{T} \qquad \textit{Eq. 2)}$$

where

$$G^{-g} = [G^T G]^{-1} G^T \qquad \textit{Eq. 3)}$$

3. Then, the estimated data error of travel time errors (e_T) can be simply obtained as:

$$e_T = \Delta \mathrm{T} - \mathrm{G} \cdot dS^{est} \qquad \textit{Eq. 4)}$$

Assuming the data error follows a Gaussian distribution, then its standard deviation can be estimated as

$$\sigma_T = \sqrt{\sum_{i=1}^{m} \frac{(\Delta \mathrm{t}_{ij} - \sum_{k=1}^{2} G_{i,k} dS_k)^2}{m-1}} \qquad \textit{Eq. 5)}$$

4. Assuming a data covariance matrix C_d follows

$$C_d = \begin{bmatrix} (\sigma_T)^2 & 0 & \cdots & 0 \\ 0 & (\sigma_T)^2 & \ddots & \vdots \\ \vdots & \ddots & \ddots & 0 \\ 0 & \cdots & 0 & (\sigma_T)^2 \end{bmatrix} \quad \textit{Eq. 6)}$$

we can then obtain the model covariance matrix C_m , i.e. the covariance matrix for the slowness errors, as

$$C_m = G^{-g} C_d (G^{-g})^T \quad \textit{Eq. 7)}$$

5. Then we draw samples of (dS_{jx}, dS_{jx}) pairs from the multivariate Gaussian distribution defined by C_m, and bootstrap the slowness-enhanced backprojection, in which error terms of slowness errors are considered.

6. Finally, for each high-frequency radiators (fig. 1a), a 2D ellipse (Fig. S11) is fitted as the confidence interval of BP location errors.

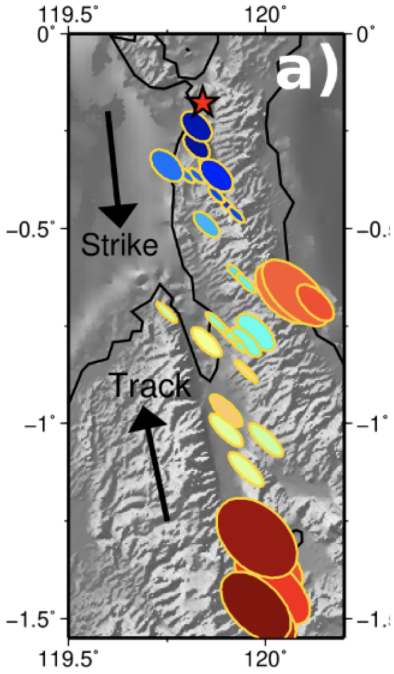

Figure S11. Confidence intervals of locations of high-frequency radiations. Color represents rupture time with respect to the mainshock origin time as Figure 1a. The estimated spatial uncertainties are plotted as error bars in Figure 1a.

7. To estimate the rupture speed, we assume the regression model is

$$y_i = b_1 t_i + b_2 + \epsilon_i \qquad \textit{Eq. 8)}$$

where y_i is the distance along strike (see Fig. 1d), t_i is the rupture time, ϵ_i is the error term as as represented the error bars in Figure 1d. So that we have the covariance matrix of error

$$\mathrm{Var}(\boldsymbol{\epsilon}) = \Omega = \begin{bmatrix} (\sigma_1)^2 & 0 & \cdots & 0 \\ 0 & (\sigma_2)^2 & \ddots & \vdots \\ \vdots & \ddots & \ddots & 0 \\ 0 & \ldots & 0 & (\sigma_n)^2 \end{bmatrix} \qquad \textit{Eq. 9)}$$

which enable us to more efficiently estimate $\boldsymbol{b}$ using generalized least square. The estimator $\hat{b}$ is then given by

$$\hat{b} = (T^T \Omega^{-1} T)^{-1} (T^T \Omega^{-1} y) \qquad \textit{Eq. 10)}$$